Adapting a propeller noise model for aircraft at cruising altitudes

David M. BLUNT[1]; Adrian JONES[2]; David MEWETT[3]

[1] Aerospace Division, Defence Science and Technology Organisation, Australia

[2] Maritime Division, Defence Science and Technology Organisation, Australia

[3] National Security & ISR Division, Defence Science and Technology Organisation, Australia

ABSTRACT

An existing propeller harmonic noise model is adapted to incorporate the effects of a stratified atmosphere so that predictions can be made of the ground-level noise for an aircraft flying at cruising altitudes. Specifically, the speed of sound and the atmospheric absorption are both made functions of altitude. The effects of refraction and ground reflection are examined, but deemed small enough to exclude from the initial model adaptation. The adapted model is applied to long-range acoustic data for a turboprop aircraft at three different cruising altitudes. The results show that a relatively good fit can be found between the model and the experimental data at the Doppler-shifted blade passing frequency within a range of source radiation angles from 30° to 110° with respect to the aircraft's direction of travel. The results also highlight the influence of molecular oxygen on the atmospheric absorption of the propeller harmonics. Recommendations are made for further improvements to the model.

Keywords: Aircraft, Propeller, Noise, Model
I-INCE Classification of Subjects Number(s): 13.1.1, 24.2, 24.6, 24.9, 75.9, 76.9

1. INTRODUCTION

The principal noise component that can be heard from turboprop aircraft at cruising altitudes at or above 3000 m (10 000 ft.) are the Doppler-shifted tone at the propeller Blade Passing Frequency (BPF) and its low-order harmonics. This is because:

   a) the propeller noise predominantly consists of a fundamental tone at the BPF, plus a series of diminishing-amplitude harmonics of this tone (1);
   b) the BPF component typically has a very high source-level amplitude and a relatively low frequency, typically around 100 Hz; and
   c) the atmosphere effectively acts as an acoustic low-pass filter; i.e. there is significantly more atmospheric absorption at higher frequencies than lower frequencies (2, 3).

Propeller harmonic noise is known to be directional (1, 4-6). The shape of the directivity pattern depends on a number of factors, including the forward airspeed of the aircraft, the geometry of the propeller blades (e.g. straight or swept), and the installation effects (e.g. nacelle or wing interactions).

This paper begins with a description of how an existing theoretical model for propeller harmonic noise has been adapted to incorporate the effects of a stratified atmosphere. This is followed by a section on the experimental data and how these were obtained. The model is then fitted to the data and the results are discussed. Finally, some conclusions and recommendations for further work are made.

2. THEORY

2.1 Propeller Harmonic Noise Model

In the helicoidal surface theory model for propeller harmonic noise developed by Hanson (7), and subsequently simplified by Parry and Crighton (8), the far-field harmonic noise of a single propeller is

---

[1] David.Blunt@dsto.defence.gov.au
[2] Adrian.Jones@dsto.defence.gov.au
[3] David.Mewett@dsto.defence.gov.au

a function of the radiation angle, θ, measured with respect to the propeller axis, and the slant range to the receiver at the time that the sound was emitted, r. If the aircraft passes directly over the receiver during straight and level flight, and the propeller axis is assumed to be parallel to the direction of flight, then the radiation angle, θ, will be equal to the elevation angle, ϕ, as shown in Figure 1. The model is assumed to apply equally well to the multi-engine case.
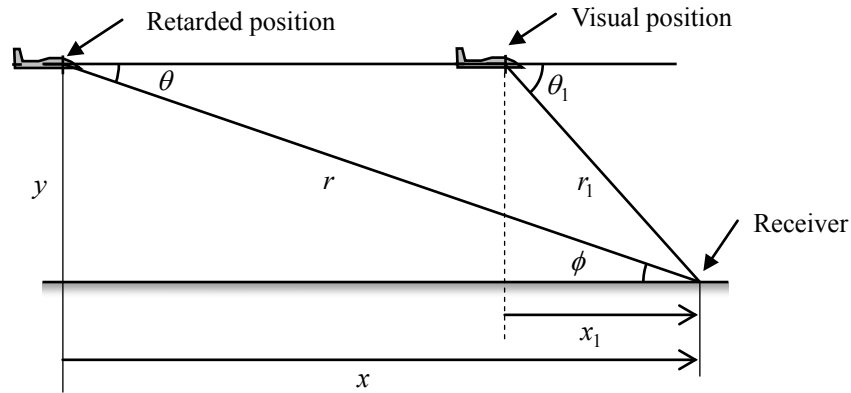
Figure 1 – Relationship between the visual position at the time that the sound is received to the retarded position at the time that the sound was emitted (adapted from (1))

Hanson's equations (7) incorporate the effects of propeller blade geometry and forward airspeed, but ignore any installation and inflow effects. In general, his model uses monopole, dipole and quadrupole sources distributed over a helicoidal surface corresponding to the in-flight path of the propeller blades through the air to predict the far-field noise. Respectively, these sources generate the blade volume displacement (thickness) noise, the blade surface force (loading) noise, and the flow disturbance noise around the blades. For sufficiently thin or swept blades operating below transonic speeds, the dipole loading sources dominate, with smaller contributions from the monopole thickness sources. The quadrupole sources only become significant at transonic speeds and are generally ignored. In the following subsonic analysis, only the dominant dipole loading sources are considered.

Parry and Crighton (8) use asymptotic approximations of the integrals in Hanson's model in order to obtain a simpler analytical equation for the far-field noise. Their main assumption in deriving this equation is that the propeller is multi-bladed, or to be more precise, that the product of the number of blades, B, and the harmonic of the blade pass frequency, m, is high. However, they demonstrate that the difference between the asymptotic approximation and the full numerical calculation can be within a few decibels (dB) for values as small as $mB = 4$ when the blade tip speed is less than Mach 0.8. They present equations for the straight-blade and swept-blade cases, but only the straight-blade case is used here as it is simpler to implement, and because the exact geometry of the propeller blades that generated the experimental data is unknown (except for the diameter and number of blades).

From Parry and Crighton (8), the asymptotic approximation of the contribution, P_m, (from the loading sources) of the mth harmonic to the sound at a distant point is

$$P_m \approx \frac{\overline{S} \exp[mB(\tanh \beta_t - \beta_t)]}{(2\pi mB \tanh \beta_t)^{1/2}} \frac{\nu!}{(mB \tanh \beta_t)^{\nu+1}}, \tag{1}$$

$$\text{where} \quad \beta_t = \text{sech}^{-1}\left[\frac{M_t \sin \theta}{(1 - M_x \cos \theta)}\right], \tag{2}$$

and the sound pressure amplitude, p_m, of the mth harmonic is

$$p_m = \frac{\rho c^2 DB}{8\pi\, r(1 - M_x \cos \theta)} P_m. \tag{3}$$

In these equations: θ is the radiation angle from the propeller axis to the receiver at the time that the sound left the source, known as the "retarded angle" (Figure 1); M_t and M_x are the Mach numbers of the blade tip and aircraft forward motion respectively; ρ is the density of the air at the source; c is the ambient speed of sound at the source; D is the diameter of the propeller; and r is

the slant range to the receiver at the time that the sound was emitted.

Parry and Crighton (8) assert that the far-field noise is dominated by the relative distribution of sources near the propeller blade tips. The values of $\bar{S}$ and v in Equation 1 are parameters describing the assumed distribution of sources in this region, which they approximate using

$$S(z) = \bar{S}(1 - z)^v \quad \text{as} \quad z \to 1, \tag{4}$$

where z is the blade span-wise/radial station normalised by the radius of the propeller. In their paper (8), the values of $\bar{S}$ and v are obtained by matching Equation 4 to the "tip variation of the radial loading distribution to be used in the full-numerical calculation." However, as the gradient of the tip loading is unknown for the experimental data used in this paper, it is assumed that the loading is uniform; i.e. that $S(z)$ is independent of z, and hence $v = 0$ in Equation 1. The value of $\bar{S}$ is derived from a least-square fit of Equation 3 to the measured data using the procedure outlined in §4.

The directivity pattern generated by Equation 3 peaks at $\theta = 90°$, and is symmetrical about this angle, for $M_x = 0$; i.e. at zero forward airspeed. However, the peak moves to lower angles, and the pattern becomes increasingly asymmetrical as the forward airspeed increases. The retarded angle, θ, is related to the visual angle, θ_1 (i.e. the angle at which the aircraft is seen when the sound is received), through (as shown by (1))

$$\cos\theta = \cos\theta_1\left(\sqrt{1 - M_x^2 \sin^2\theta_1}\right) + M_x \sin^2\theta_1. \tag{5}$$

2.2   Doppler Effect

The Doppler shift for a moving source and a stationary receiver is (as shown by (1))

$$\frac{f_o}{f_s} = \frac{1}{(1 - M_x \cos\theta)}, \tag{6}$$

where f_o is the observed frequency and f_s is the source frequency.

Equations 2 and 3 include Doppler-shift factors, and these factors directly influence the noise directivity pattern. However, it should be noted that the actual frequency of each harmonic is not explicitly included in these equations. This frequency only becomes important when determining the amount of atmospheric absorption that the sound experiences (see Section 2.5).

2.3   Speed of Sound

The overall speed of sound from a source to a receiver is comprised of the speed of sound in the air, which is essentially a known function of temperature (see, e.g. Annex A of (2)), plus the relative speed of the air towards the receiver. Temperature and wind speed profiles can be measured using weather balloons or other devices, and the effects can be combined into a single sound-speed profile.

Generally, the speed of sound is significantly lower at altitude than it is at ground level. Hence, a compromise value for c must be found. Since the presence of c in Equations 1–3 (both explicitly and in the Mach numbers) essentially arises from the time delay between when the sound is emitted and when it is received, the value for c needs to be based on an estimate of the actual delay under non-uniform sound-speed conditions. The simplest way to do this is to divide the atmosphere into N layers, where the speed of sound is assumed to be constant in each layer, but can vary between the layers. The total time delay, τ, ignoring refraction (i.e. along a straight path) is then

$$\tau = \sum_{i=1}^{N} \frac{d_i}{c_i \sin\theta}, \tag{7}$$

where for the ith layer, d_i is the layer thickness and c_i is the speed of sound in that layer. If the thickness of each layer is the same, this can be rewritten as

$$\tau = \frac{Nd}{\sin\theta}\left(\frac{1}{N}\sum_{i=1}^{N}\frac{1}{c_i}\right). \tag{8}$$

Equation 8 is simply the slant range multiplied by the average of the inverse speed of sound over the uniform-thickness layers. Hence, the inverse-averaged speed of sound, c_a, can be defined as

$$c_a = \left(\frac{1}{N} \sum_{i=1}^{N} \frac{1}{c_i} \right)^{-1}. \tag{9}$$

This value of c_a has been used in place of c in Equation 3, and also to compute the Mach numbers M_t and M_x in Equations 2 and 3.

2.4   Atmospheric Refraction

Atmospheric temperature and wind gradients can produce significant refractive effects (1). Negative gradients (that cause the speed of sound to decrease with altitude) bend the sound away from the ground. In the limit, it is possible for a sound ray to travel in an arc that just grazes the ground. This produces an acoustic shadow zone behind in which there is minimal sound penetration (Figure 2).
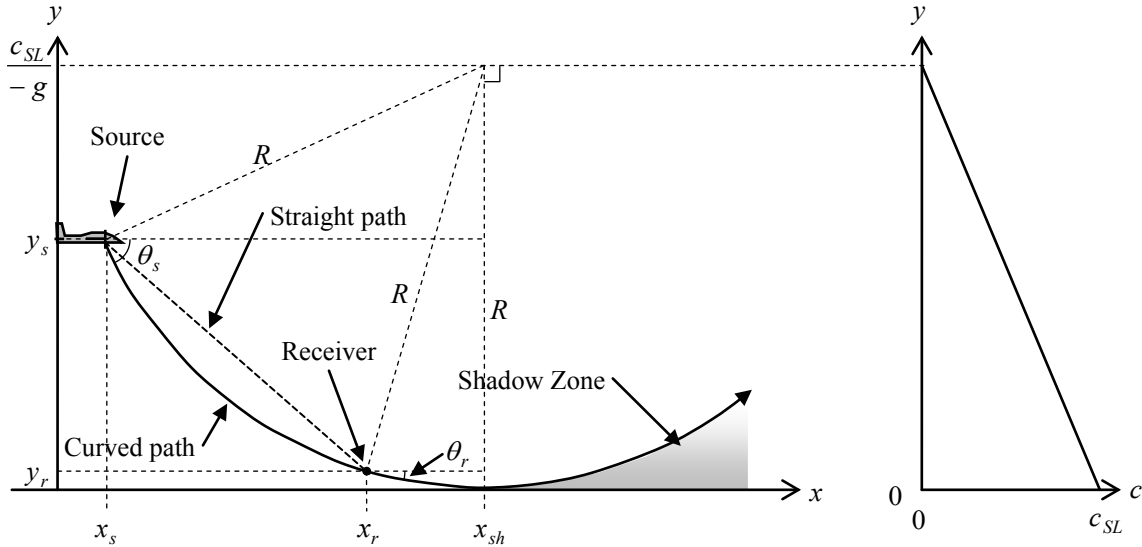

Figure 2 – Refracted sound ray (left) in a negative linear sound-speed gradient (right)

Ignoring the wind, the U.S. Standard Atmosphere (9) shows a near-linear decline in the speed of sound from sea level (c_{SL}) up to about 10 000 m (33 000 ft.). The speed of sound can therefore be approximated by

$$c \approx c_{SL} + gy, \tag{10}$$

where the gradient, g, is negative.

It can be shown that linear sound-speed gradients cause sound rays to travel in circular arcs with a radius of curvature given by (10)

$$R = \left(\frac{c_{SL}}{-g} - y_s \right) \frac{1}{\cos \theta_s}, \tag{11}$$

where θ_s is the initial source ray angle with respect to the horizontal at altitude y_s. Note that $R \to \infty$ as $\theta_s \to 90°$. It follows that, for a sound ray passing from a source at altitude (x_s, y_s) to a receiver near the ground (x_r, y_r),

$$y_s - y_r = R(\cos \theta_r - \cos \theta_s), \text{ and} \tag{12}$$

$$x_s - x_r = R(\sin \theta_s - \sin \theta_r), \tag{13}$$

where θ_r is the final received ray angle with respect to the horizontal at altitude y_r.

The length along the curved path is

$$l_{sr} = R(\theta_s - \theta_r). \tag{14}$$

The ground range from the source to the shadow zone can be calculated from

$$x_{sh} - x_s = \frac{c_{SL}}{-g} \sin \theta_s, \text{ where } \theta_s = \cos^{-1} \left(1 + \frac{gy_s}{c_{SL}} \right). \tag{15}$$

Using the values of $c_{SL} = 340$ m.s^{-1} and $g \approx -0.004$ s^{-1} from the U.S. Standard Atmosphere, the predicted shadow zone for a source at 3048 m (10 000 ft.) would begin at a ground range of 22 km, and increase for higher altitudes. This range is well beyond the range of the recorded experimental data and the presence of any shadow zones can be safely ignored.

From (10), the time for sound to travel from the source to the ground along the grazing ray is

$$\tau_c = \frac{1}{g} \ln\left(\frac{\cos\theta_s}{1 + \sin\theta_s} \right). \tag{16}$$

Hence, the travel time from the source to the receiver is

$$\tau_{sr} = \frac{1}{g} \ln\left(\frac{\cos\theta_s \left(1 + \sin\theta_r\right)}{\cos\theta_r \left(1 + \sin\theta_s\right)} \right). \tag{17}$$

Typical effects of refraction (excluding wind) are shown in Table 1. It can be seen that the differences in path lengths and travel times are both very small ($\ll$1%). As both these effects are deemed negligible, only the straight path is used in the following analysis. However, it should be noted that the differences between the source radiation angles could become important at longer ground ranges due to the distortion this may impose on the source directivity pattern. Further analysis of this effect would be worthwhile but has not been conducted here due to time constraints.

Table 1 – Typical effects of refraction in the U.S. Std. Atmosphere (linear-sound-speed gradient approx.) for a source moving in a straight & level path directly over a receiver 1.7 m above the ground

Source Altitude	Variable		Ground Range		
			1000 m	5000 m	10 000 m
	Source radiation angle (θ_s)	Curved path (deg.)	81.03	52.38	34.85
		Straight path (deg.)	80.68	50.63	31.36
		Difference (deg.)	0.35	1.75	3.49
6096 m (20 000 ft.)	Path length (l_{sr})	Curved path (m)	6175.8	7884.1	11718.0
		Straight path (m)	6175.8	7882.9	11710.7
		Difference (m)	0.0	1.2	7.3
	Travel time (τ_{sr})	Curved path, (s)	18.85	24.05	35.72
		Straight path (s)	18.85	24.06	35.74
		Difference (s)	0.00	−0.01	−0.02

2.5　Atmospheric Absorption

In this work, the atmospheric absorption is calculated from weather balloon sounding data using the method described in Annex A of ISO 9613-1 (2). Annex A of this standard provides equations for:

    a)　the absorption caused by the transport processes of "classical" physics (α_{cl}),

    b)　the molecular absorption caused by rotational relaxation (α_{rot}),

    c)　the molecular absorption caused by the vibrational relaxation of oxygen ($\alpha_{vib,O}$), and

    d)　the molecular absorption caused by the vibrational relaxation of nitrogen ($\alpha_{vib,N}$).

The overall attenuation coefficient, α, (in units of dB/m) is the sum of the above four terms, i.e.

$$\alpha = \left(\alpha_{cl} + \alpha_{rot}\right) + \alpha_{vib,O} + \alpha_{vib,N}. \tag{18}$$

In ISO 9613-1, the α_{cl} and α_{rot} terms are combined into a single function of the atmospheric pressure and temperature, and the frequency of the sound. The $\alpha_{vib,O}$ and $\alpha_{vib,N}$ terms are functions of the frequency of the sound, the speed of sound, and the relaxation frequencies of oxygen and nitrogen respectively. These relaxation frequencies are in turn functions of pressure, temperature and the molar concentration of water vapour. It should be noted that the $\alpha_{vib,O}$ and $\alpha_{vib,N}$ terms are generally much larger than the $\alpha_{cl} + \alpha_{rot}$ term.

2.6　Ground Reflection

The interference pattern generated by the ground reflection depends on the ground impedance and the path length difference between the direct and reflected sound rays. An example for an acoustically "hard" flat horizontal surface (where there is no phase change at the point of reflection) is shown in

Figure 3. This pattern is derived for a source passing in a straight line directly over a receiver and is independent of altitude. It is symmetrical about the Closest Point of Approach (CPA), which is at 90°.
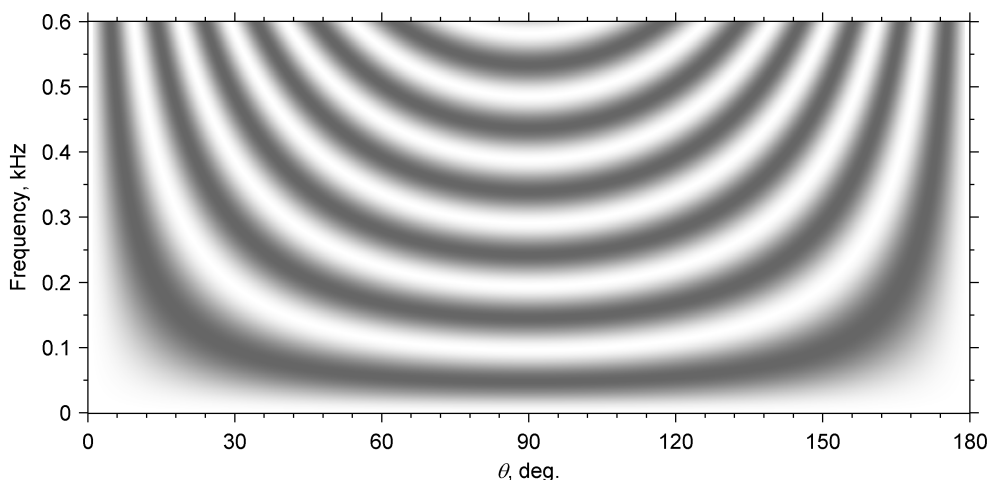

Figure 3 – Ground reflection interference pattern for an aircraft moving in a straight line directly over a receiver (c_a = 330 m/s, receiver 1.7 m above the ground)

For simplicity, and because the ground impedance for the experimental data (Section 3) is unknown, ground reflection effects have been left out of the model. The experimental data are therefore expected to show departures from the model predictions over localised elevation angles (Section 4). The expected effect of a 100% reflection from an acoustically hard flat surface is shown in Figure 4. Here, 100% amplitude corresponds to the strength of the direct sound wave. The asymmetry (about 90°) is due to the Doppler shift of the propeller harmonics. It can be seen that maxima for all three harmonics are expected near angles of 36° and 96°. In between these angles there is partial reinforcement of the 1× BPF component, but significant cancellation of the 2× and 3× BPF components. The strength of the actual ground reflection and its effect would, of course, be smaller than that shown in Figure 4. Variations in the positions of the peaks and troughs would also be expected if the ground is not perfectly flat.
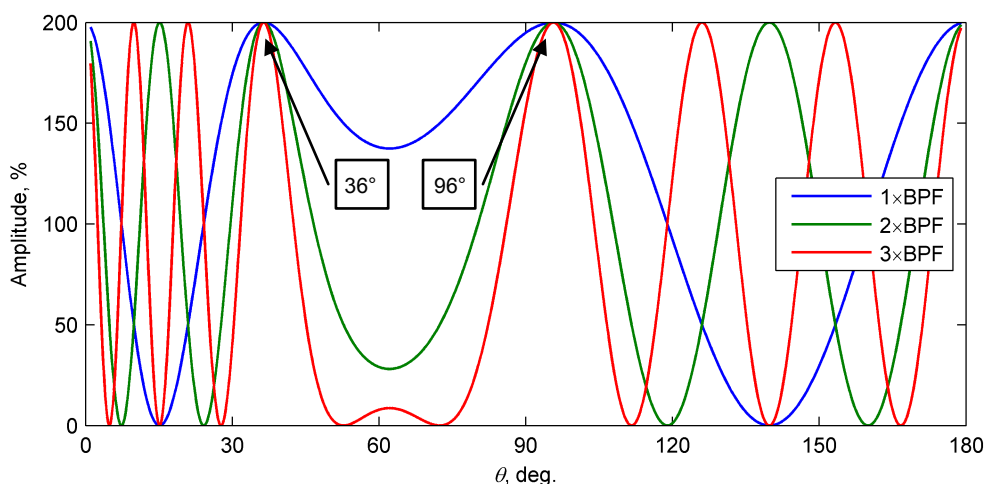

Figure 4 – Expected effect of a 100% reflection from the ground on the propeller harmonic amplitudes (receiver 1.7 m above the ground)

3. EXPERIMENTAL DATA

The experimental data were obtained from a multi-engine turboprop aircraft in straight and level flight at a constant airspeed (high-speed cruise). The aircraft flew a cross (+) pattern over the ground-level microphones where the intersecting legs were at 90° to each other. This pattern was repeated at three different cruising-level altitudes (denoted low, medium & high). Each altitude serial

consisted of one upwind, one downwind, and two crosswind legs. These nominal directions were fixed on the direction of the wind at ground level. However, the wind direction and speed varied with altitude.

Three Brüel & Kjær microphones (two 4189-A-021, and one 4188-A-021) were mounted on tripods 1.7 m above ground level and about 10 m apart on the top of a small rise in an otherwise flat landscape with only low vegetation. This location was at the centre of the cross flown by the aircraft. The microphones pointed up and were essentially omnidirectional at the frequencies of interest (i.e. < 1 kHz) to a high degree of accuracy (< 0.25 dB) (11). Spherical 90 mm diameter foam windshields were used to minimise any wind-induced noise.

The track of the aircraft was recorded at one-second intervals using a Global Positioning System (GPS) logger in the aircraft. The logger also collected the GPS time signal, which was used to synchronise the position of the aircraft with the acoustic recordings (as described in Section 4).

The atmospheric data were collected from a weather balloon sounding near the time of the acoustic recordings. The data were interpolated using the MATLAB 'pchip' function (piecewise cubic interpolation) to provide a uniform vertical spacing. The resulting upwind–downwind speed profile is shown in Figure 5, and reveals significant atmospheric stratification. A similar plot was obtained for the crosswind profile, but is not shown here due to space restrictions.
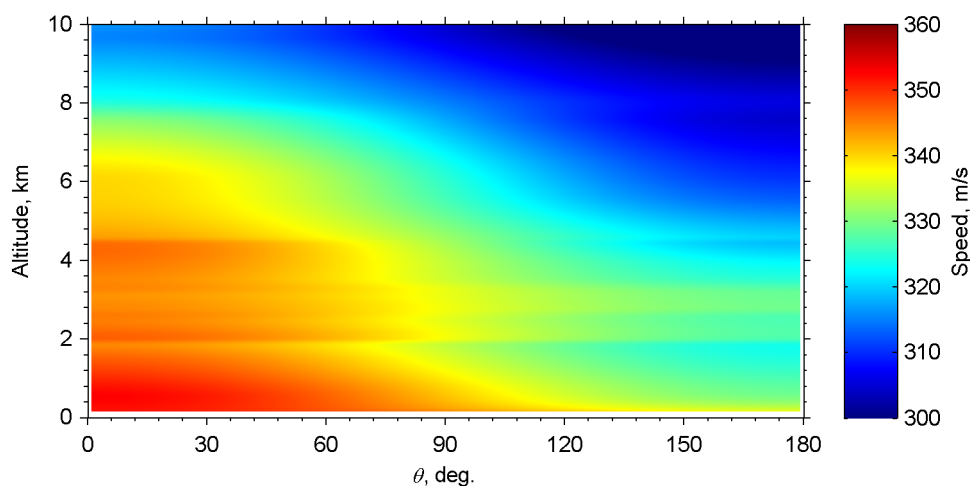

Figure 5 – Speed of sound (including the wind component) in a straight line from the source to the receiver for the downwind (0°→180°) and upwind (180°→0°) directions

Typical atmospheric absorption coefficients for the Doppler-shifted propeller harmonics are shown in Figure 6. This figure clearly illustrates the low-pass filtering characteristic of the atmosphere. The regions of high absorption occur where the Doppler-shifted harmonics approach the relaxation frequency of oxygen. The relaxation frequency of nitrogen is only close to the BPF harmonics at altitudes below 3000 m (10 000 ft.). The effects illustrated in Figure 6 are consistent with those reported by Ingard (12, §9.6.3 *Attenuation Due to Absorption (Vibrational Relaxation)*).

4. RESULTS

The propeller harmonic noise model was fitted to the experimental data in the following manner:
  a) The slant range from the microphone location (measured using a handheld GPS receiver) to the aircraft was calculated from the aircraft GPS data.
  b) The time delay for the sound to travel in a straight path from the aircraft to the microphone was computed from the slant range and the inverse-averaged speed of sound obtained from the appropriate sound speed profile (e.g. from Figure 5).
  c) The computed time delay was added to the GPS time to estimate the time that the sound was received by the microphones. This provided a suitable time axis for the GPS position data in the microphone frame of reference.
  d) Sound pressure levels (SPL) were plotted against frequency and time in spectrograms for each leg of each altitude serial.
  e) The amplitudes and frequencies of the Doppler-shifted propeller harmonics were extracted from the spectrograms using a frequency-tracking algorithm. This provided 12 SPL traces

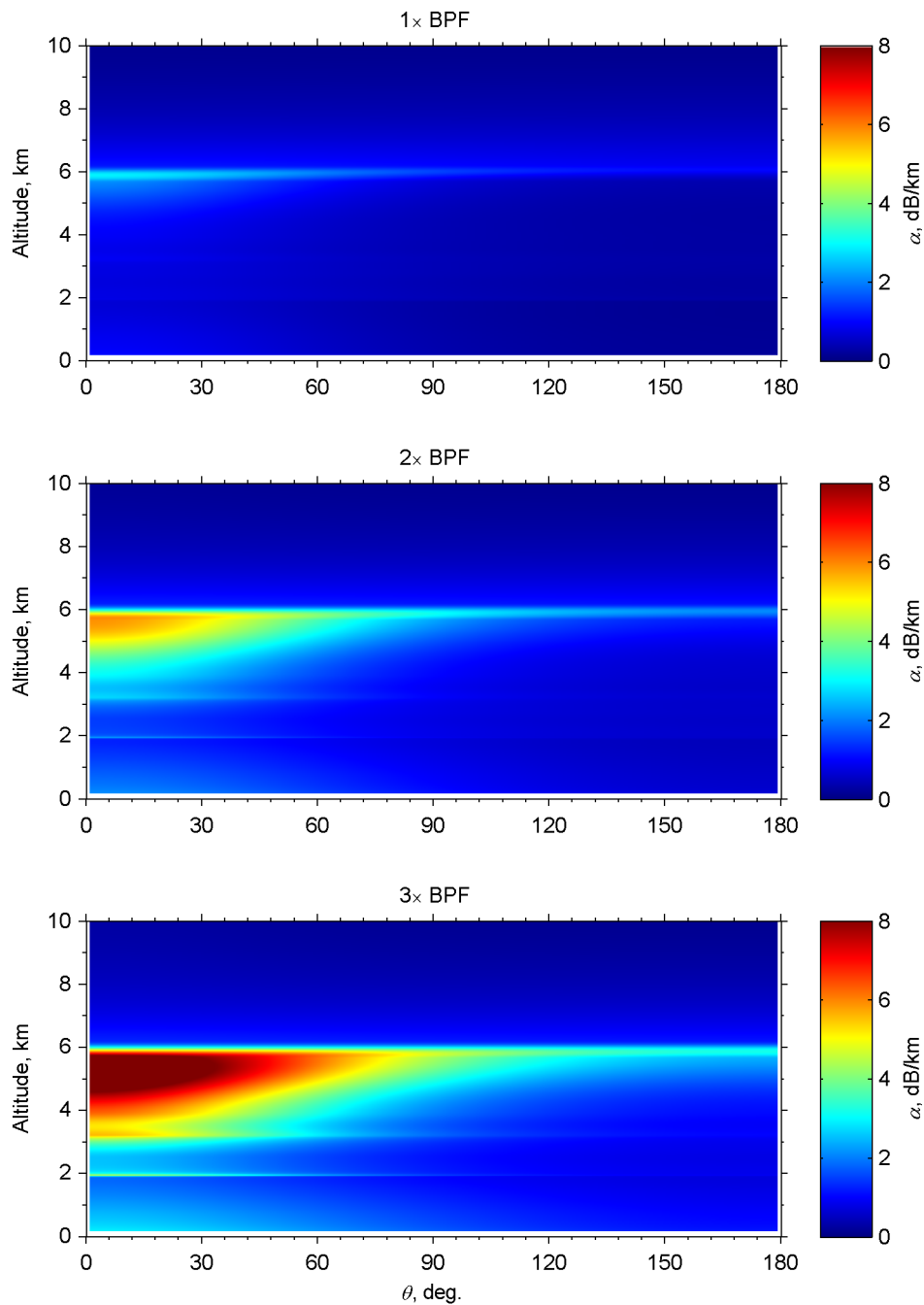for each harmonic at each altitude (3 microphones × 4 legs).

Figure 6 – Typical atmospheric absorption coefficients at the Doppler-shifted propeller harmonics – the areas of high absorption are caused by the proximity of the Doppler-shifted harmonics to the relaxation frequency of molecular oxygen

f) The ground range and elevation of the aircraft for each trace point were estimated using the time-delayed GPS position data (from Step c). This allowed the SPL traces to be plotted against the radiation angle, θ, as shown in Figure 7. All 12 traces for each harmonic at each altitude are overlaid in this figure.

g) The extracted Doppler-shifted frequencies were used to calculate the atmospheric absorption coefficients for each atmospheric layer using the properties for that layer obtained from the interpolated weather balloon data. These were very similar to those shown in Figure 6. The coefficients were averaged across the layers and multiplied by the slant range to obtain the overall absorption along a straight path from the source to the

receiver.

h) The value of $\bar{S}$ was obtained from a least-square fit of Equation 3 to the traces shown in Figure 7, adjusted for the absorption computed in Step g). The bold curves) in Figure 7 show the predicted values for p_m using the fitted values of $\bar{S}$, adjusted for atmospheric absorption.

It can be seen from Figure 7 that the best model fit occurs at the fundamental BPF between radiation angles of 30° and 110°. At angles just below this range, the model tends to under-predict the measured BPF amplitudes at the low and medium altitudes (there being virtually no data outside the 30°−110° range at the high altitude). This could be the result of refraction effects, or the influence of blade thickness noise at these low angles (8). The results just above 110° also show a slight under-prediction, although the evidence is weaker here. Refraction effects are less likely at this higher angle (closer to perpendicular), and reinforcement from the ground reflection is still expected up to around 120°.
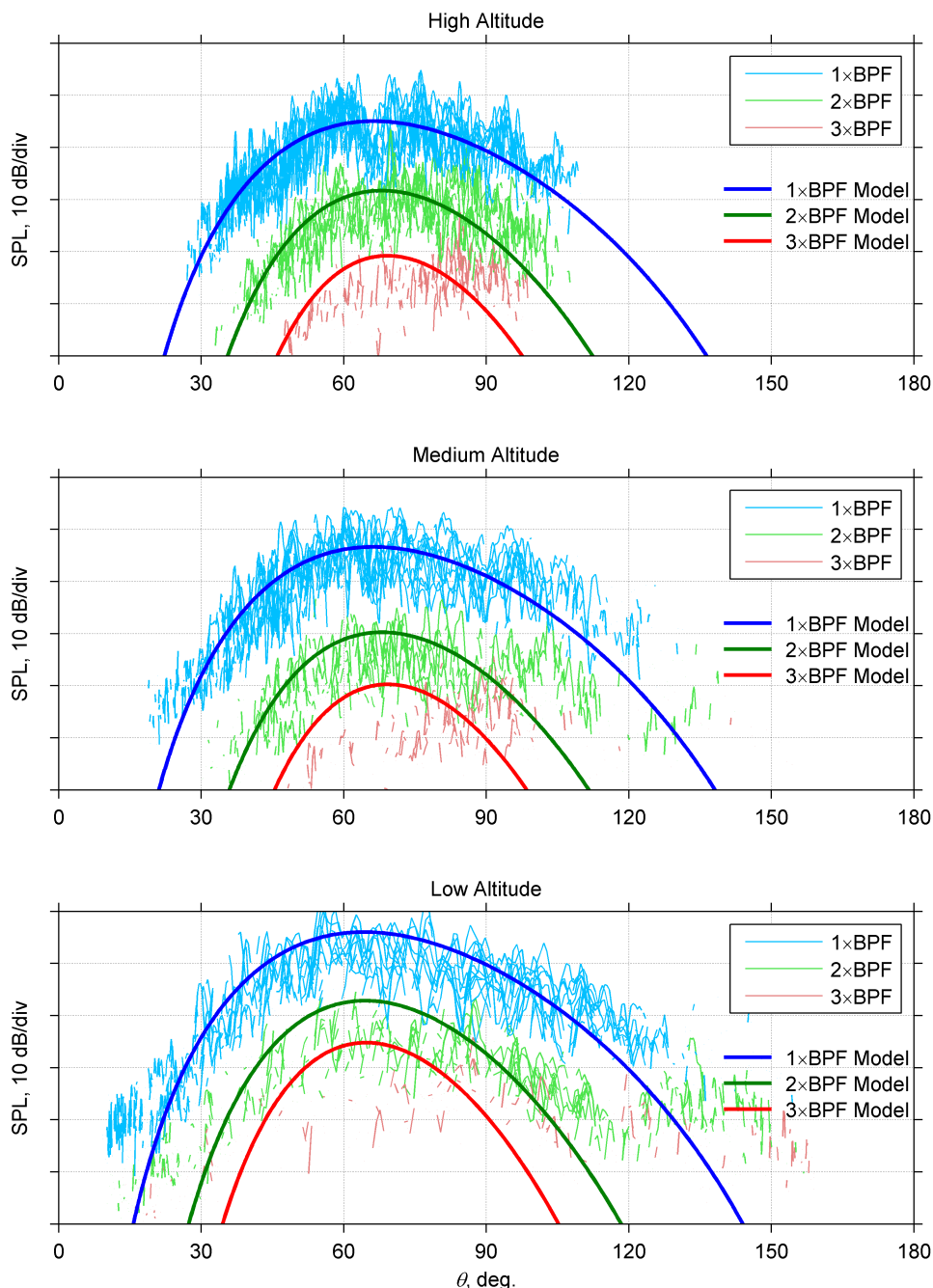

Figure 7 – Measured (unweighted) propeller harmonic noise levels (feint traces) and least-square fit model predictions (bold curves) – the curves reflect the predicted directivity pattern of the propeller loading noise adjusted for atmospheric absorption and peak between angles of 65°−70°

The fits for the 2× and 3× BPF components are slightly less convincing, particularly at angles above 120°. In order to obtain reasonable fits near the peaks (65°–70°), the data outside the ranges of 30°–120° and 45°–105° had to be excluded for the second and third harmonics respectively. However, these harmonics are expected to be more influenced by ground reflection effects (Figure 4), and there is evidence of this in the results (e.g. dip in 2× BPF near 120° & rise near 140°). The model could therefore be improved by including a function to calculate the expected interference pattern from the known geometry (i.e. the slant range and elevation angle, assuming flat ground). The reflection coefficient could be estimated during the least-square fitting stage (i.e. at Step h). Alternatively, the effects of the ground reflection could be minimised using microphones flush with the ground surface (or mounted inverted over a plate embedded in the ground).

5. CONCLUSIONS

A theoretical model for propeller harmonic noise has been adapted to estimate the relative ground-level sound pressures of aircraft flying at cruising altitudes. The predicted harmonic amplitudes show a particularly good fit with the experimental data at the Doppler-shifted fundamental BPF for elevation/radiation angles of 30°–110°. Notable features of this work are:

a) The measured tonal levels appear to adhere to the predictions of a model which is only based on loading forces; i.e. thickness noise and other noise sources are less important.

b) Refraction effects only appear to be significant at low elevation angles; e.g. $\theta < 30°$. However, further investigation of these effects, particularly the effective distortion of the propeller source directivity pattern at these angles is recommended.

c) The effect of atmospheric absorption on the Doppler-shifted propeller harmonics is very important, particularly the component caused by the relaxation of molecular oxygen.

d) Ground-reflection effects are significant and it is recommended that these are incorporated into the model in order to obtain better results, particularly at the 2× and 3× BPF components, or that microphones flush with the ground are used for future experiments.

ACKNOWLEDGEMENT

REFERENCES

1. Magliozzi B, Hanson DB, Amiet RK. Propeller and Propfan Noise. In: Hubbard HH, editor. Aeroacoustics of Flight Vehicles: Theory and Practice. NASA Reference Publication 1258, WRDC Technical Report 90-3052. Vol. 1: Noise Sources: NASA; 1991.
2. ISO 9613-1. Acoustics - Attenuation of sound during propagation outdoors. Part 1: Calculation of the absorption of sound by the atmosphere: International Organization for Standardization; 1996.
3. ISO 9613-2. Acoustics - Attenuation of sound during propagation outdoors. Part 2: General method of calculation: International Organization for Standardization; 1996.
4. Block PJW, Gentry GL, Jr. Directivity and Trends of Noise Generated by a Propeller in a Wake. NASA Technical Paper 2609. Langley Research Center, Hampton Virginia, 1986.
5. Marte JE, Kurtz DW. A Review of Aerodynamic Noise from Propellers, Rotors and Lift Fans. Jet Propulsion Laboratory, California Institute of Technology, 1970 Technical Report 32-1462.
6. Willshire WLJ. Noise Propagation from a Four-Engine Propeller-Driven Airplane. Hampton, Virginia: NASA Langley Research Center, 1987 NASA Technical Memorandum 89035.
7. Hanson DB. Helicoidal Surface Theory for Harmonic Noise of Propellers in the Far Field. AIAA Journal. 1980;18(10):1213-20.
8. Parry AB, Crighton DG. Asymptotic Theory of Propeller Noise - Part I: Subsonic Single-Rotation Propeller. AIAA Journal. 1989;27(9):1184-90.
9. U.S. Std. Atm. U.S. Standard Atmosphere, 1976. 1976.
10. Tolstoy I, Clay CS. Ocean Acoustics: Theory and Experiment in Under-Water Sound: McGraw-Hill; 1966.
11. Microphone Handbook Vol. 2. Technical Documentation. Denmark: Brüel & Kjær, 1995 BA 5105–12.
12. Ingard U. Notes on Acoustics. Hingham, Massachusetts: Infinity Science Press; 2008.